Application of proper orthogonal decomposition (POD) to investigate a turbulent boundary layer in a channel with rough walls

M. SEN [a], Kiran Bhaganagar [a] & V. Juttijudata [b]

[a] Department of Mechanical Engineering , University of Maine ,
Orono, ME, USA

[b] Department of Aerospace Engineering , Kasetsart University ,
Bangkok, Thailand
Published online: 02 Nov 2009.

PLEASE SCROLL DOWN FOR ARTICLE

Application of proper orthogonal decomposition (POD) to investigate a turbulent boundary layer in a channel with rough walls

M. SEN†, KIRAN BHAGANAGAR*† and V. JUTTIJUDATA‡

†Department of Mechanical Engineering, University of Maine, Orono, ME, USA
‡Department of Aerospace Engineering, Kasetsart University, Bangkok, Thailand

Snapshot proper orthogonal decomposition (POD) is used to investigate a rough-wall turbulent boundary layer in a channel. One- and two-dimensional POD decompositions have been performed using 3D velocity database from direct numerical simulations (DNS). DNS of a turbulent channel flow with rough walls consisting of 3D roughness elements have been performed at $\mathrm{Re}_\tau = 180$. 1D analysis has revealed that convergence of the POD for a rough wall is slower compared to the smooth wall, which is attributed to the increase in range of length scales due to roughness. For the egg-carton roughness elements, the depth of a roughness sublayer (ζ^n_{mode}) for POD mode n decays with increasing mode number in an exponential manner as $\zeta^n_{\mathrm{mode}} = 14\mathrm{e}^{-0.86n}h$ for roughness of height h. The reconstruction of turbulence intensities and shear stress has revealed that the inner layer which includes the roughness sublayer is well captured by first 10 POD modes. 2D POD analysis has revealed that roughness alters the size and spacing of the large scale, energy containing structures of the flow.

Keywords: Roughwall; Direct numerical simulation; Turbulent boundary layers

1. Introduction

Proper orthogonal decomposition (POD) proposed by Lumley [32] to objectively identify the coherent structures in a turbulent flow has contributed significantly to our understanding of a smooth-wall turbulent boundary layer (TBL). POD [8, 32, 33, 47] extracts a complete, orthogonal set of spatial eigenfunctions (i.e. modes) from the measured second-order correlation function. These POD eigenmodes provide an optimal basis of expansion of the flow in the sense that energy convergence is more rapid than any other linear representation. The combination of the most energetic POD modes are associated with the large-scale, energy containing structure of the flow.

One of the earliest applications of the POD was proposed by Bakewell and Lumley [6]. They extracted the POD of the wall region from the two-point correlations of a single velocity component based on experimental fully developed pipe flow data. Herzog [20] used the same facility as Bakewell and Lumley [6] to perform a fully three-dimensional study of the wall region. Moin and Moser [37], Sirovich *et al.* [7, 47–49] thoroughly studied the coherent structures from the POD based on numerical fully developed channel flow data. Sirovich *et al.* [48, 49] extracted the POD modes using snapshot POD, a modification of direct POD. The snapshot POD has the distinct advantage of being computationally efficient as it uses the

correlation of instantaneous snapshots of the flow and thus reduces the order of the eigenvalue problem to that of the number of snapshots and not the physical mesh.

In the bulk of these applications, the POD has been used to analyze the experimental and computational data with a view to extracting dominant features and trends in the flow. These studies have demonstrated that 90% of total energy can be captured by the first 10 dominant POD modes in wall-bounded flows with a smooth surface. The studies have further identified the coherent structures consisting of pairs of counter-rotating streamwise vortices which produce a strong updraft of low-speed fluid away from the wall and a more gentle downdraft of high-speed fluid toward the wall.

Surface roughness in a turbulent flow has been studied extensively, yet much continues to be unknown regarding the flow structures and the nature and extent of influence of surface roughness on turbulent flow. For the egg-carton roughness, our prior analysis of the rough-wall turbulence mechanisms has revealed increased turbulence activities, and well-correlated velocity fluctuations at the rough-wall side [11]. Compared to the smooth wall, different turbulence structures were observed in the rough-wall region, especially stronger streamwise vortices close to the roughness elements. We further investigated whether there is a fundamentally different self-sustaining process (SSP) by which turbulence is maintained in a rough-wall turbulent boundary layer, and the analysis has revealed that SSP (quasi-streamwise rolls and near-wall streaks) of near-wall turbulence in the rough-wall channel is similar to that of the smooth-wall channel. The only additional effect of surface roughness is due to kinematic effects due to the presence of surface roughness. POD will serve as an effective tool to obtain a clear understanding of the nature of these structures.

Unlike a smooth wall, the turbulence generation for a rough wall can also take place through mechanisms other than SSP. For example, for mesh screen roughness [48], it was argued that it is unlikely for self-sustaining mechanisms to survive, the turbulence generation occurs through some other mechanisms (to date, the exact nature of this mechanism is still controversial). However, two-point correlations have confirmed the existence of well-correlated structures. Mesh-roughness creates high levels of turbulence by enhancing the absolute fluctuation levels hence higher turbulent kinetic energy). Well-correlated structural patterns have been reported by various researchers (e.g., [5, 35])

To date, we do not have a general consensus on the strength or size of these structures or the mechanisms for the generation of these structures. In some roughness configurations, the existence of these structures is unlikely. The mechanisms of turbulence production might be different from the smooth wall. For example, it was shown that one possible driving mechanism of the near-wall vortical structures is related to the normal velocity fluctuations in the plane of the crests [40, 41]. In some other cases, for the drag reducing configurations such as riblets it has been established that they produce a damping action on these structures. Nevertheless, in any of these roughness configurations, based on our current understanding of rough walls, it is obvious that there are more scales than just k or d (e.g., [11, 14, 21]). In general, rough-surface creates (with exception of some configurations; e.g., riblets) a higher turbulence level (TKE), serves as efficient agents in enhancing mixing, produces high drag (frictional and form drag components), and has confirmed the presence of well-correlated structures. For any roughness geometry, POD allows us to evaluate the distribution of energy as a function of scale. It decomposes the flow field into modes having various scales. POD captures the well-correlated spatial patterns, in the sense, the structures that contribute to the TKE. Comparison of convergence rates, POD modes and the reconstruction of the TKE from these modes will provide an effective tool to understand the influence of roughness geometry on flow physics. In addition, as the TKE can be captured by a fraction of the total modes so it results in reduced order of the system. Thus, the instantaneous velocity can be reconstructed only by a fraction of these modes.

Another motivation of the POD study is to make progress toward the long-term goal of obtaining a classification of rough wall based on physics rather than k- or d-type classification. For example, a new parameterization was proposed where it was demonstrated that the roughness function is proportional to the wall normal velocity an the plane of the roughness crest [40, 41]. POD decomposition of the flow field provides the modes that contribute to the TKE. By comparison of the rough- and smooth-wall modes, the number of the modes that are influenced by the roughness (such as inhomogenous effects), and the nature of the modification of these structures can be obtained.

In a turbulent boundary layer, viscosity is dominant in the viscous sublayer (VSL) and most of the turbulence generation happens in the buffer region, the region of self-sustaining process (SSP). By assuming $y+$ (wall distance scaled in wall-units) can be viewed as a local Reynolds number, the thickness of the viscous sublayer (VSL) can be interpreted as a critical Reynolds number, which will increase due to a stabilizing influence (e.g., riblets [16]) and decrease due to a de-stabilizing one (e.g., adverse pressure gradient and roughness). VSL thickness defines the $y+$ at which the VSL and log region intersect. Thus, the VSL and critical Re argument can be used as a guideline, for example, how the constant in the log-description of the mean velocity (wall-function boundary conditions) should be altered to account for roughness effects.

We define a roughness sublayer (RSL) as the region above the roughness is which the flow is influenced by the individual roughness elements and is therefore not spatially homogenous (i.e. the time averaged statistics are not independent of locations, at the same mean wall-normal distance). If the roughness is small (and within the viscous sublayer layer) then the inhomogeneity or RSL is within VSL. However, if the height of roughness is larger than a few wall units, the RSL extends beyond the VSL and way into the buffer region, as the depth of RSL increases with the height of the roughness in a proportional manner. Unlike the depth of VSL, RSL for canonical roughness is more complicated, as the depth of this layer exhibits a dependence on the roughness geometry. Further, the interaction of roughness elements (kinematics effect) and the turbulence (dynamical effects) is very dominant in the roughness sublayer. Further, there is no clear cut mathematical theory to obtain the depth of RSL, and thus has remained an open question in rough-wall research.

An estimate of roughness sublayer has been obtained as the height of layer above the roughness where the mean velocity profile departs from the logarithmic profile law from the experiments of Perry *et al*. [43] Raupach *et al*. [44], Mulhearn [38]. The analysis by Bhaganagar *et al*. [11, 12] has revealed that the extent of inhomogeneity is sensitive on the statistical parameter being measured. It was shown that the roughness sublayer defined by the pressure fluctuations (ζ_p) is larger than that defined by rms of velocity fluctuations (ζ_q), and much larger than that defined by the rms of vorticity fluctuations (ζ_ω). As the dominant POD mode represents the dynamical features of the flow, an estimate of the depth of roughness sublayer for the dominant POD mode (ζ_{mode}^1) will provide a better understanding of the extent of influence of roughness on the dominant energy containing features of the flow. A similar analysis for the higher POD modes will provide an estimate of ζ_{mode}^n for mode n. Based on these results, we will be able to address an important question of the range of energy containing structures that are directly influenced by roughness resulting in inhomogeneity of the flow statistics. Having a realistic estimate of the depth of the roughness sublayer is also important for parameterization in turbulence models and even LES.

In the outer region of the turbulent boundary layer, it is still not clear if roughness modifies the dynamically active features of the flow. On the one hand, the experiments of Krogstad *et al*. [25], Tachie *et al*. [51], Keirsbulk *et al*. [23], George and Simpson [18], Bhaganagar *et al*. [11] have demonstrated that significant differences are discernible in the turbulence velocity statistics *throughout* the boundary layer. On the other hand, the results of Perry
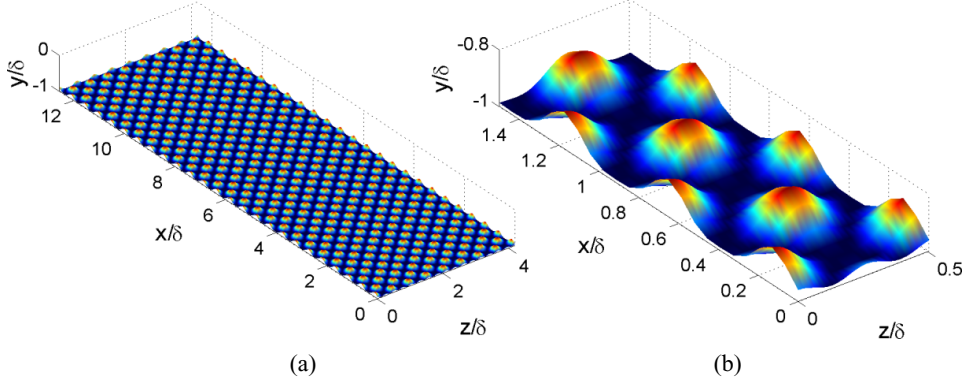
Figure 1. (a) The channel is shown from the lower wall ($y/\delta = -1$) to its centerline ($y/\delta = 0$) with roughness surface of $h^+ = 21.6$. The streamwise and spanwise roughness-element periods are respectively $l_x/\delta = 2\pi/10$ and $l_z/\delta = 2\pi/16$, which correspond to $l_x^+ = l_x u_\tau^s/\nu = 251$ and $l_z^+ = 157$, (b) A portion of the lower rough wall to highlight the roughness peaks and valleys.

et al. [43], Raupach *et al.* [44], Shafi and Antonia [50] demonstrate a similarity of velocity and vorticity statistics in the outer region between the rough- and smooth-wall boundary layers.

To get a clearer understanding of the extent of influence of roughness on dynamical features of the flow, we perform snapshot POD analysis. The database for the analysis is obtained from DNS of turbulent flow in a channel with rough walls consisting of 3D roughness elements arranged in an "egg carton" pattern (see figure 1). The three-dimensional velocity database has been used to construct the two-point correlations in time (C). An eigenvalue problem is formulated with C as the kernel. The solution of the eigenvalue problem gives the temporal coefficients and their corresponding eigenvalues. The velocity field is then projected onto these temporal coefficients to obtain the corresponding spatial POD modes. Each of these modes is considered to represent the dynamically active structures. Reconstruction of turbulent intensity and shear-stress is performed based on first few POD modes to capture the dynamics of turbulence—a significant consequence for turbulence modeling.

An estimate of the length of roughness sublayer based on POD modes is obtained as follows: As the roughness elements in the horizontal *x*–*z* plane are represented by the double sine function, the POD is performed at two different inhomogeneous locations—the 'peak' and the 'valley' regions of roughness bumps as shown in figure 1. The underlying assumption is that by performing POD at these two extreme locations, we can get a good estimate of the extent of inhomogeneity present in the layer. Plane averaging over a repeating unit of a uniform array will lead to a representative profile within the roughness sublayer, which could then be regarded as spatially homogeneous on scales larger than the unit, if it is much larger than the lateral size of individual elements. This type of unit averaging has been done by Raupach et al. [44], Wood and Mason [55] and Cheng and Castro [15].

We also perform a 2D POD analysis in the *y*–*z* and *x*–*y* planes to understand the nature of the coherent structures. We are particularly interested to determine how roughness alters the size and spacing of the coherent structures as represented by the 2D eigenfunctions. It should be noted that the present analysis is specific to the roughness elements where the underlying turbulence generation mechanisms are similar to that of the smooth wall. Future work needs to be performed to understand the nature of POD structures for different scenarios of turbulence generation mechanisms.

The paper is organized as follows: section 2 deals with the DNS methodology used to generate the vast database to construct the temporal two-point correlation matrix ($C(t, t')$) and description of the POD methodology to extract the modes. In section 3 we discuss the results. We present results for one-dimensional POD, followed by the analysis to obtain depth of roughness-sublayer. It should be noted that for small roughness heights (as in the present case), the roughness sublayer is part of the inner layer. In cases such as meteorological flows with large roughness heights (e.g., buildings), the roughness sublayer can extend into the outer layer, and the analysis will be more complicated than that presented here. Next we present the results and analysis for 2D POD in the *y*–*z* plane followed by 2D POD in the *x*–*y* plane. This is followed by a summary in section 4.

2. Numerical methodology

2.1 *Direct numerical simulations*

DNS was performed by Bhaganagar *et al.* for a channel with a lower rough wall and an upper smooth wall [11]. This tool has been modified to simulate the flow in a channel with both upper and lower rough walls. DNS was performed using a parallel (message-passing interface) implementation of a plane-channel code that employs a Fourier spectral discretization in the streamwise *x* and spanwise *z* directions, and a fourth-order compact-finite- difference scheme in the wall-normal *y* direction. The Navier–Stokes equations were solved in the vertical-velocity and vertical-vorticity formulation [10]. The time advancement is done with a Crank–Nicolson method for the viscous terms and a third-order low-storage Runge–Kutta scheme for the others. The surface roughness is represented by the immersed boundary method, which imposes the three-dimensional 'egg-carton'-shaped surface on the lower wall of the channel shown in figure 1. In units of the channel half-width δ, with respect to the Cartesian coordinate system shown in figure 1 (note that $y = 0$ corresponds to the channel centerline and $y = -1$ to the (unused) smooth lower wall, above which the immersed boundary method is applied), the virtual no-slip surface $\sigma(x, z)$ is given by

$$\sigma(x, z) = \sigma_0 + \frac{h}{4}\left[-1 + \left(1 + \sin\left(\frac{2\pi x}{l_x} + \frac{2\pi z}{l_z}\right)\right)\left(1 + \sin\left(\frac{2\pi x}{l_x} - \frac{2\pi z}{l_z}\right)\right)\right], \quad (1)$$

where *h* is the (peak to valley) roughness height, l_x and l_z are the streamwise and spanwise wavelengths (peak-to-peak distance) of the roughness elements, and σ_0 defines the mean offset of the immersed boundary; the present results use $\sigma = -0.96$. For this surface, the roughness 'bumps' extend $3h/4$ above σ_0, while the valleys lie $h/4$ below it. The virtual roughness surface is prescribed according to the immersed-boundary methodology [56], by adding an appropriate body-force term to the momentum equations to enforce the no-slip condition on $\sigma(x, z)$. The simulations are performed at $Re_\tau = 180$ on a mesh of size $192 * 129 * 192$.

2.2 *POD implementation*

For a detailed treatment of POD methodology, the reader is referred to literature [9, 32, 48, 49]. In this section, we will focus on the actual procedure used in this work to obtain the POD modes. We follow the same procedure as outlined by Sirovich [47]. The data used for the POD analysis in the present investigation consist of 3D fluctuating velocity fields, i.e. (u_1, u_2, u_3) in the entire 3D domain. The fluctuating velocity fields have been derived by subtracting the mean

velocity from the instantaneous velocity obtained from the DNS. The DNS domain consists of $N_x = 192$ points in the streamwise (x) direction, $N_y = 129$ points in the wall-normal direction, and $N_z = 192$ in the spanwise (z) direction. The instantaneous velocity fields are collected for nondimensional time of 30 time units (in terms of u_τ and δ) separated by 0.04 time units, after the flow has reached statistical equilibrium. Each 3D velocity field at given time instant will be referred to as a snapshot, the total number of snapshots being N_t. The POD is performed for the half-channel. The sample size used in the ensemble averaging procedure is enhanced by imposing the symmetries inherent in the flow. As the flow is invariant under vertical reflection, and also under spanwise reflection. The sample size is increased two-folds by imposing the above-mentioned symmetries.

1D POD decomposition in the wall-normal (y) direction is performed to extract the three components of the 1D eigenfunction $\phi_u(y)$, $\phi_v(y)$, $\phi_w(y)$. Given the velocity profiles at all (x, z) locations and at all times, the temporal correlation function between snapshots t and t' is defined as

$$C(t, t') = \frac{1}{N_t} \int_y u_i(y, t) u_i(y, t') \mathrm{d}y, \quad i = 1, 3. \tag{2}$$

The numerical evaluation of the above integral is performed using trapezoidal rule, similar to the approach of Moin and Moser [37]. The temporal correlation function ($C(t, t')$) is then used as a kernel to formulate the eigenvalue problem:

$$\int C(t, t') a^n(t') \mathrm{d}t' = \lambda_n a^n(t). \tag{3}$$

Solution of the eigenvalue problem will result in the temporal coefficients (which are eigenvectors of the correlation tensor), $a^n(t)$, and eigenvalues, λ^n, for mode number n. 1D spatial eigenmodes are then calculated by projecting the temporal coefficients onto the velocity field as

$$\phi_i^n(y) = \sum_{p=1}^{N_t} a^n(t_p) u_i(y, t_p), \quad i = 1, 3. \tag{4}$$

Here ϕ_u^n, ϕ_v^n and ϕ_w^n correspond to the streamwise, wall-normal and spanwise eigenmodes or eigenfunctions, respectively. Eigenvalues obtained from the solution of the eigenvalue problem will represent the energy content of each mode. As the fluctuating components of velocity fields have been used for the calculation of velocity correlation tensor, the sum of eigenvalues will represent the turbulent kinetic energy (TKE), and the eigenvalue of each mode will correspond to fraction of the TKE contained in that mode. The mode with the largest eigenvalue is referred to as the dominant POD.

For the 2D y–z POD, the above 1D POD analysis can easily be extended. 2D POD decomposition is performed to extract the three components of the 2D eigenvectors $\phi_u(y, z)$, $\phi_v(y, z)$, $\phi_w(y, z)$. Given the instantaneous velocity in the y–z plane at all x locations and at all times the temporal two-point correlation matrix ($C(t, t')$) is constructed.

A eigenvalue problem is formulated with the temporal auto-correlation, $C(t, t')$, as the kernel, the solution of which gives the temporal coefficients, $a^n(t_p)$. The 2D spatial eigenmodes are constructed as

$$\phi_i^n(y, z) = \sum_{p=1}^{N_t} a^n(t_p) u_i(y, z, t_p), \quad i = 1, 3 \tag{5}$$

where $\phi_u(y, z)$, $\phi_v(y, z)$, and $\phi_w(y, z)$ correspond to the three components of the 2D eigemodes. The 2D POD decomposition in the x–y plane is performed in a similar manner.

Table 1. Convergence tests with increasing number of snapshots for 1D POD of smooth- and rough wall.

Number of snapshots	λ_1/TKE (smooth)	λ_1/TKE (rough)
10	0.7337	0.2684
100	0.3835	0.1769
200	0.3535	0.1779
500	0.3107	0.1740
1000	0.2788	0.1876
2000	0.2755	0.1847
3000	0.2764	0.1818
4000	0.2859	0.1818
5000	0.2859	0.1816
6000	0.2858	0.1815

3. Results

The DNS simulations for a channel with rough walls have been used to compute the two-point correlation tensor, which we will refer to as the rough-wall case. In order to understand the relative effect of roughness, we performed DNS on a channel with smooth walls, and data have been used to compute two-point correlation tensor, which we will refer to as the smooth-wall case.

3.1 *Convergence tests*

Convergence checks of the POD were performed for increased spatial and temporal resolution, as well. Based on spatial convergence tests, an optimal number of $N_x = 12$, $N_z = 8$, $N_y = 65$ for 1D POD and $N_x = 24$, $N_z = 48$, $N_y = 65$ for 2D POD have been used. Table 1 shows the dominant eigenvalue with increasing number of snapshots. The POD analysis has been performed with 6000 snapshots for both rough and smooth wall.

For validation of the POD tool, we performed POD for smooth wall and compared the eigenvalues and eigenvectors with the existing literature. Table 2 shows the energy captured by the first, second and third POD modes, and the number of modes required to capture 90% of TKE. Our results for 1D smooth wall compare well the results of Moin and Moser [37]. Also shown in the table is the results for 1D rough wall. The energy captured by the first POD mode for rough wall is less than the energy captured by the smooth wall. Furthermore 90% of TKE is captured by dominant 10 POD modes for smooth wall, whereas it requires 22 modes for the rough wall. The first four eigenvectors for smooth wall also compare well with the existing literature. This is discussed in depth in the results section.

Table 2. Comparison of eigenvalues (first, second and third) and the total number of modes to capture 90% of TKE for 1D POD: the 1D PODs of Moin and Moser for smooth wall [37] are compared with our results of 1D POD for smooth- and rough wall.

Case	λ_1/TKE	λ_2/TKE	λ_3/TKE	λ_4/TKE	Modes for 90% of TKE
1D POD of Moin and Moser [37]	0.32	0.16	0.08	–	10
Current results 1D POD smooth wall	0.28	0.16	0.085	0.05	10
Current results 1D POD rough wall	0.18	0.10	0.09	0.067	22

3.2 *DNS results*

In order to ensure the reliability of the data before performing the POD, the turbulence statistics were analyzed. As the rough surface is arbitrary, in order to have a clear cut estimate of the location of the rough wall, we define a virtual offset α for the rough side. This is done by expressing the mean velocity (U) normalized by friction velocity (u_τ) in the log-region in the following form:

$$\frac{U}{u_\tau} = \frac{1}{\kappa} \ln \frac{(y - \alpha)}{y_0}. \tag{6}$$

Here, α is the virtual offset, y_0 is the roughness length, and y_0 and α are determined by fitting the mean velocity profile in the inertial sublayer to the above equation. u_τ is the local wall-shear velocity (i.e., u_τ of each wall). For the smooth-wall case, u_τ is obtained using the definition of shear at the upper smooth wall, and for the rough wall u_τ is obtained exactly from the balance of the mean momentum equation at the rough wall. All the distances are measured from the virtual offset for the rough wall. y^+ is used to represent the distance from the wall in wall units. All the results denote y^+ taking the virtual offset into account and using u_τ.

Figure 2(a) shows the mean velocity profile normalized by the wall-shear velocity plotted in wall units for the smooth- and rough walls. In this figure, y^+ represents the distance from the wall scaled in wall-units. The roughness produces the expected downward shift in U of 5.31. Raupach *et al.* [44] present a relationship between ΔU^+ (U^+ scaled by u_τ) and h^+ (roughness height scaled by u_τ and channel half height) for different roughness geometries. For our h^+ of 36, the corresponding ΔU^+ is around 5.5. This result also serves as a good validation for our numerics.

Figure 2(b) shows root-mean-square (rms) velocity fluctuations normalized by u_τ. It is plotted against the distance from the wall y_w normalized by δ_t. We define δ_t as the distance from the wall to the y location corresponding to the minimum rms velocity fluctuations. It takes into account the virtual offset for the rough wall. The maximum turbulence intensity of all the three components is enhanced for the rough wall compared to the smooth wall. The location of the peak intensity shifts further away from the wall due to roughness. It should be
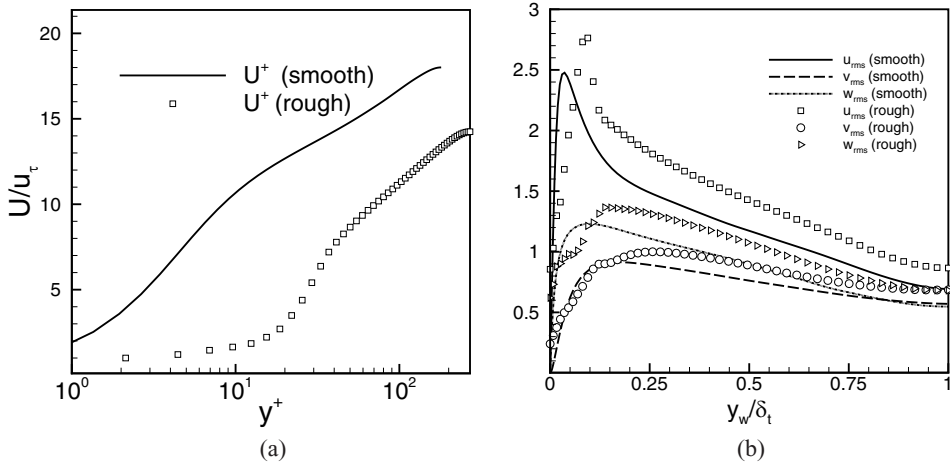

Figure 2.   (a) Mean velocity scaled by u_τ plotted in wall-units, (b) turbulent intensity of velocity components plotted vs. distance from the wall y_w scaled by δ_t.

noted that scaled in this manner, both the inner and outer layers are altered due to roughness. This behavior differs from the results of Orlandi and Leonardi [41], and this can be attributed to difference in shape and spacing of the roughness elements.

3.3 *One-dimensional POD analysis*

3.3.1 Rough-wall POD. Figure 3(a) shows the distribution of the eigenvalues over the mode number for rough-wall and smooth-wall POD. This distribution is a representation of
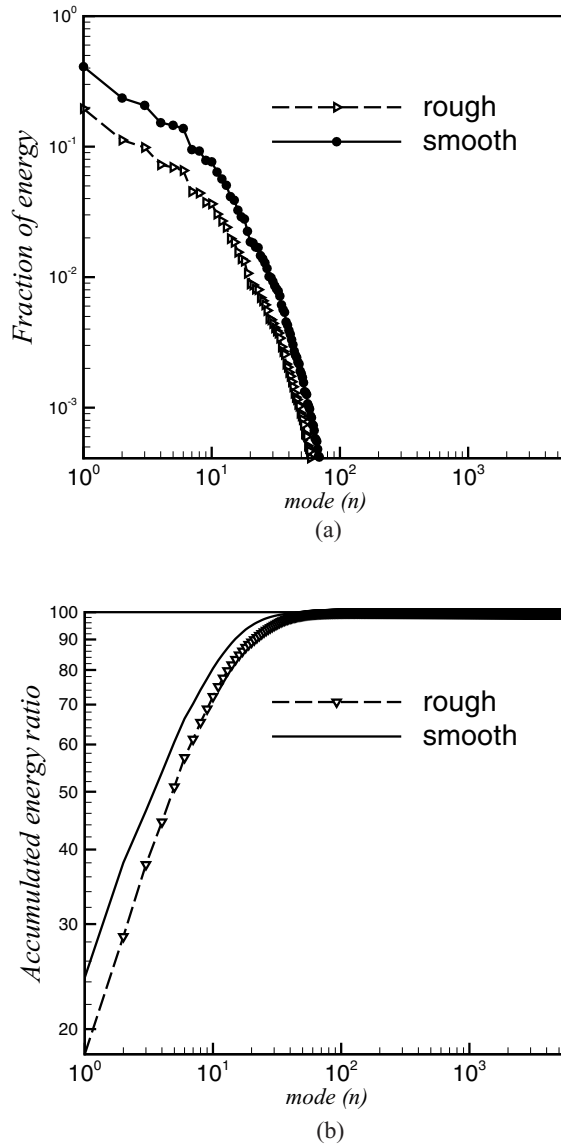

Figure 3. Eigenvalues for one-dimensional POD: (a) fractional contribution to the TKE by the POD modes for rough- and smooth-wall POD. (b) Accumulated energy ratio of modes as a function of the mode number for rough- and smooth-wall POD.

the relative energy content ($e^n = \lambda^n / \sum_{m=1}^{N_t} \lambda^m$) of the total kinetic energy (TKE) of the flow for mode n. The lower modes correspond to the larger scale, energy containing features of the flow, and the higher modes to the smaller scale, less energetic features of the flow. On comparing the rough-wall POD with smooth-wall POD, the fraction of the energy contained in the first few modes is lower for the rough wall compared to the smooth wall. Furthermore, the convergence of rough wall is slower than the smooth wall as indicated by the slower decaying rate of the eigenvalue spectrum.

The cumulative contribution of the modes to the turbulent kinetic energy can be represented by the accumulated energy ratio ($e_{accum}^n = \sum_{m=1}^{n} \lambda^m / \sum_{m=1}^{N_t} \lambda_m$). Figure 3(b) shows an accumulated energy ratio of all the POD modes. The convergence of the modes for the rough wall is slower compared to that for the smooth wall. The first three modes capture around 35% and 50%, respectively, for the rough- and smooth walls. The first 10 modes capture around 70% and 80%, respectively, for the rough- and smooth walls. Finally, 90% of the total turbulent kinetic energy is captured by 22 modes for the rough wall and around 15 modes for the smooth wall. The slower convergence of the rough wall can be attributed to an increase in the range of length scales in roughwall turbulent boundary layer.

Figure 4 shows streamwise, ϕ_u, wall-normal, ϕ_v, and spanwise, ϕ_w, components of the first four POD modes for rough- and smooth wall. The smooth-wall POD modes are qualitatively
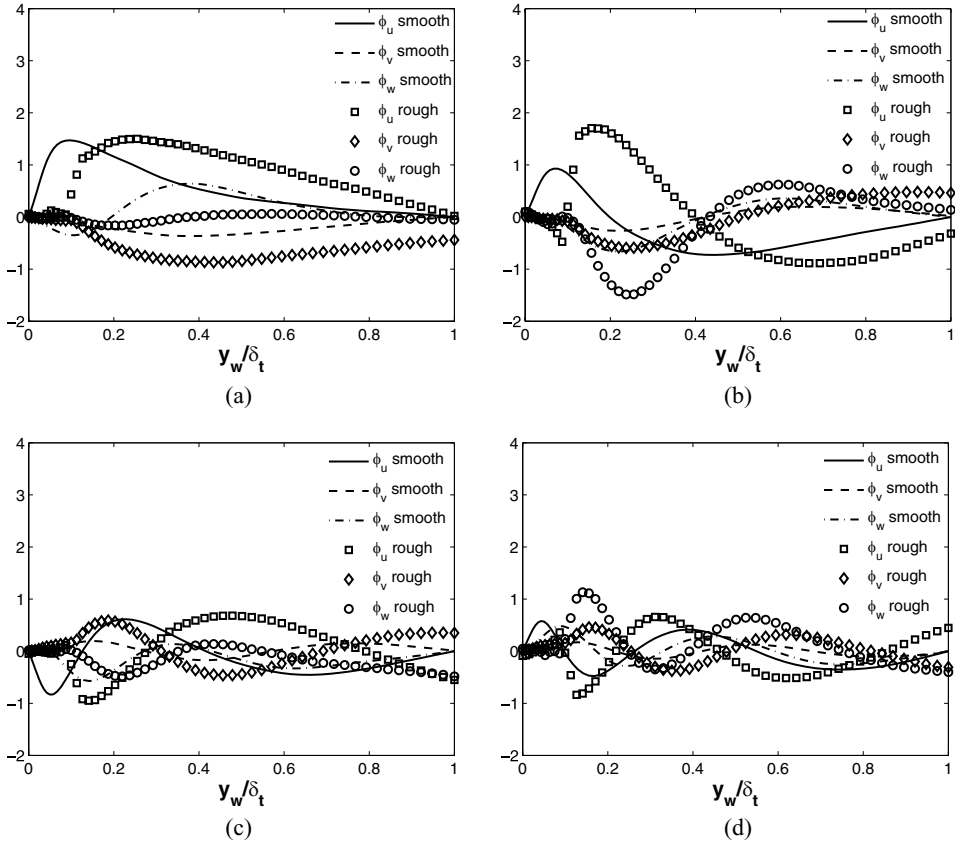

Figure 4.   Spatial eigenmodes of the 1D POD for the rough- and smooth wall: (a) mode 1, (b) mode 2, (c) mode 3 and (d) mode 4.

similar to that obtained by Moin and Moser [37] and Adrian and co-workers [29]. This also serves as a good validation for our numerics. Similar to the smooth wall, the eigenfunctions for the rough wall are localized near the wall and tend to zero near the center of the channel. From $y/\delta_t = 0$ to 0.1, due to spatial inhomogeneity, the high positive magnitude at roughness peaks is offset by the negative magnitude at the valleys resulting in net low amplitude. The eigenfunction structure of all three components, ϕ_u, ϕ_v and ϕ_w, of mode 1 exhibit significant differences for the rough- and smooth walls throughout the boundary layer. Thus, suggesting the effect of roughness is observed both in the inner and outer layers of the TBL for the dominant energy containing mode. For the first mode, the peak of ϕ_u is around y_w/δ_t of 0.1 for smooth wall and y_w/δ_t of 0.2 for the rough wall. This is in agreement with the roughness resulting in outward shift in rms velocity components. However, the zero-crossing of ϕ_v and ϕ_w for rough wall is around the same location as for the smooth wall. On comparing the spatial structures of modes 2, 3 and 4, similar trends as observed for mode 1 are present. The differences between the rough and smooth-wall POD become les conspicuous with increasing mode numbers. Qualitatively, this suggests that the influence of roughness is less apparent in the higher modes. Next, we perform a quantitative analysis to get an estimate of the effect of inhomogeneity on the POD modes.

3.3.2 Peak- and valley-POD. We perform an analysis to determine the depth of the roughness layer. We select two inhomogeneous locations the 'peak' and 'valley' regions of the roughness bump as shown in figure 1(a). We perform a 1D POD and extract POD modes at these locations which we refer to as the peak- and valley-POD, respectively. We also perform POD decomposition by computing the two-point correlations from the velocity measurements at all x and z locations, that includes the peak and valley of the roughness bump, which we refer to as the rough-wall POD. Figure 5(a) shows the fraction of energy captured by the peak- and valley-POD. Also shown in the figure is the energy fraction for the rough-wall POD (includes both the peak and valley locations), which is obtained by taking both the peak and valley locations to compute the POD modes. Some differences are observed between the peak and valley up to the first 10 POD modes. Beyond which, the differences are not apparent. Figure 5(b) shows the accumulated energy ratio for peak, valley and rough-wall POD modes. Spatial inhomogeneity is observed for the first 10 POD modes. We compare the eigenfunctions (ϕ_u) obtained from the peak-POD and valley-POD analysis to determine the extent of inhomogeneity. Figure 6 shows the first four POD modes. The first eigenmodes obtained from the peak-POD, valley-POD, POD for the rough wall and POD for the smooth wall are plotted. We also present the POD modes for smooth wall. Examining the first POD mode, it is clear that spatial homogeneity is not achieved until $y_w/\delta_t = 0.75$. We performed this for three different roughness heights ($h^+ = 5$, 10, 20 and corresponding $h/\delta_t = 0.03, 0.06$ and 0.12) and obtained the depth of the roughness layer i.e., ζ_{mode}^1 to be about $6h$. A similar examination of the second mode reveals a somewhat smaller roughness sublayer. Spatial homogeneity of this mode is achieved at y_w/δ_t of 0.25, resulting in the depth of the roughness sublayer for second mode roughness sublayer i.e ζ_{mode}^2 to be about $2h$. It is clear that the depth of the sublayer decreases with the increasing mode number. This trend continues for the third and the fourth modes as well. Spatial homogeneity for the third and fourth mode is not achieved until y_w/δ_t of 0.16 and 0.11, respectively, resulting in the depth of the roughness sublayer for third (ζ_{mode}^3) and fourth(ζ_{mode}^4) mode to be about $1.33h$ and $0.9h$, respectively. The effect of inhomogeneity is more pronounced in the first few POD modes only. Using the depth of the sublayer for these four modes, we performed data-fitting and this has resulted in an exponential power law of the form $\zeta_{mode}^n = 14h e^{-0.86n}$ for mode number n. The depth of the sublayer is almost negligible beyond the tenth mode. The peak- and valley-POD analysis has revealed the presence of strong inhomogeneity in the large-scale features of the flow. The
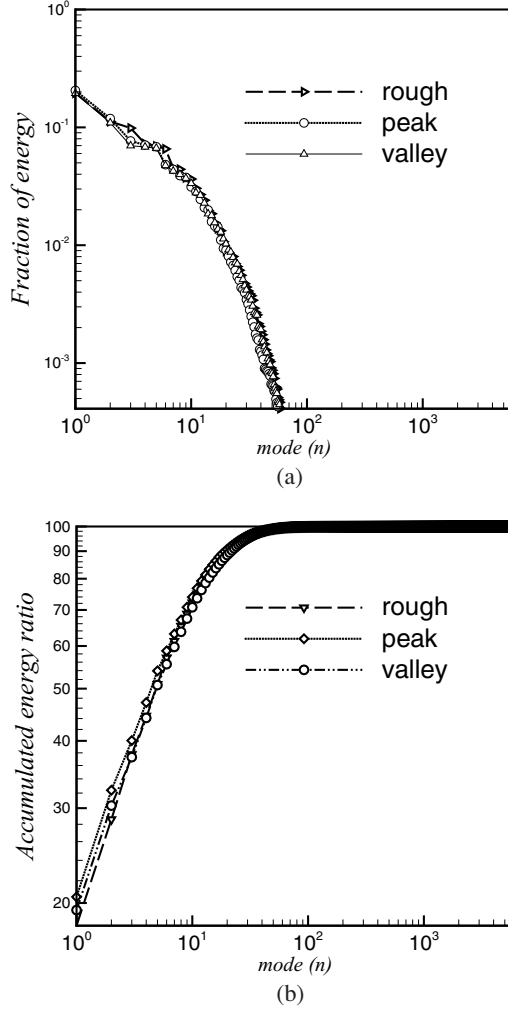
Figure 5.   Eigenvalues for one-dimensional POD: (a) eigenvalue spectrum as a function of the mode number for peak-, valley- and rough-wall POD. (b) Accumulated energy ratio of modes as a function of the mode number for peak-, valley- and rough-wall POD.

depth of the roughness sublayer gradually diminishes for the higher modes. This result is of significant consequence to low-dimensional modeling of rough-wall turbulent boundary layer community: the presence of inhomogeneity due to roughness needs to be accounted only for the dominant modes (which represent large-scale features of the flow).

3.3.3   Reconstruction.   We next reconstruct the turbulence statistics using POD modes. Velocity field at time any time instant (snapshot), t, can be perfectly reconstructed by projecting the first m temporal coefficients to the corresponding spatial mode as

$$u_i(x, y, z, t) = \sum_{n=1}^{m} a^n(t)\phi_i^n(y), \quad i = 1, 3. \tag{7}$$

Figure 7 shows the convergence of the POD modes for turbulent stresses as a function of the number of POD terms. The convergence is compared with the exact value obtained from the
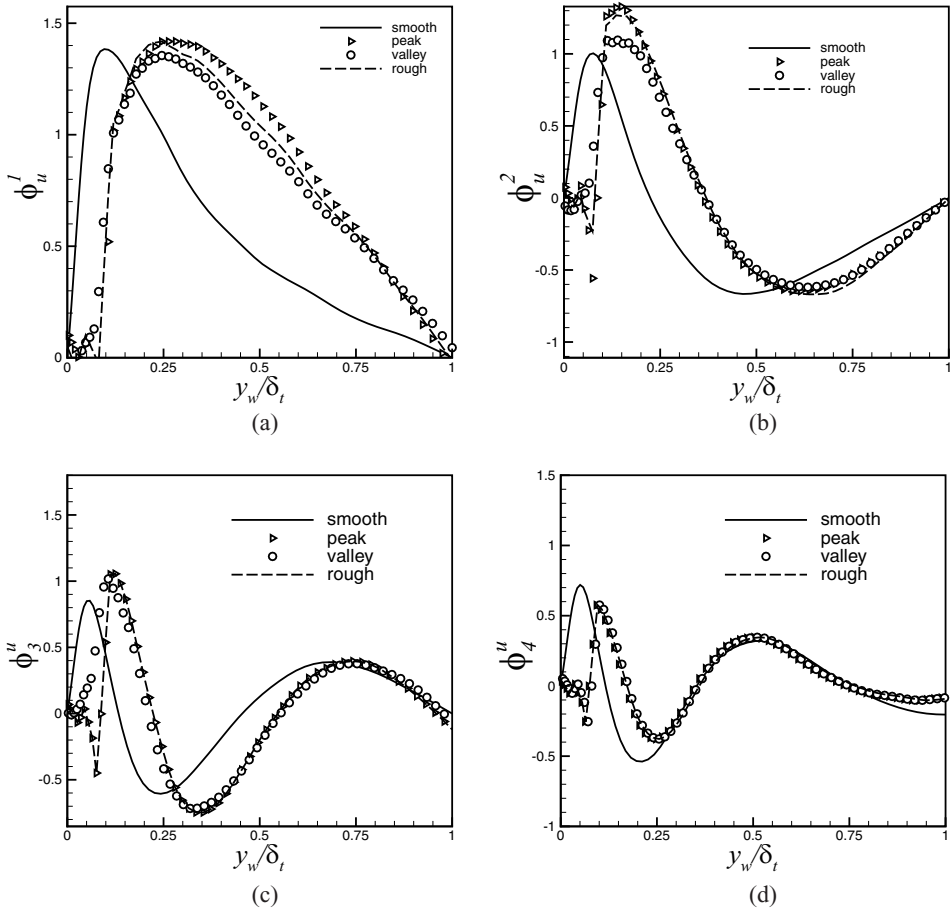
Figure 6. Comparison of the eigenfunctions (ϕ_u) from the peak-POD, valley-POD locations, rough-wall POD (constructed from both peak and valley locations) and smooth-wall POD for (a) first POD mode, (b) second POD mode, (c) third POD mode, (d) fourth POD mode.

DNS. This exact value matched well with that computed by taking all the POD modes which served as a further validation of our numerics. The velocities are nondimensionalized with u_τ. The location and the amplitude of the peak of the rms of u fluctuations is well captured by the first 10 POD modes. It is interesting that the inner-layer, which included the roughness-sublayer is well captured by these 10 POD modes. Adding additional POD modes does not change the inner layer significantly. This confirms our findings regarding the roughness sublayer that effect of inhomogeneity is captured by the lower modes. To reproduce rms of u fluctuations accurately around 50 POD modes are required. A similar trend is observed in the rms of v, w fluctuations and shear uv. As the turbulence stresses can be reconstructed using a small number of POD modes, and as the inner layer is well captured by the lower modes, it appears to be promising to develop a low-dimensional model for turbulent channel flow with rough walls.

3.4 *2D POD analysis*

In this section, we first present the results for 2D POD performed in the *y–z* plane. We are particularly interested to understand the effect of roughness on the size of the turbulence structures.
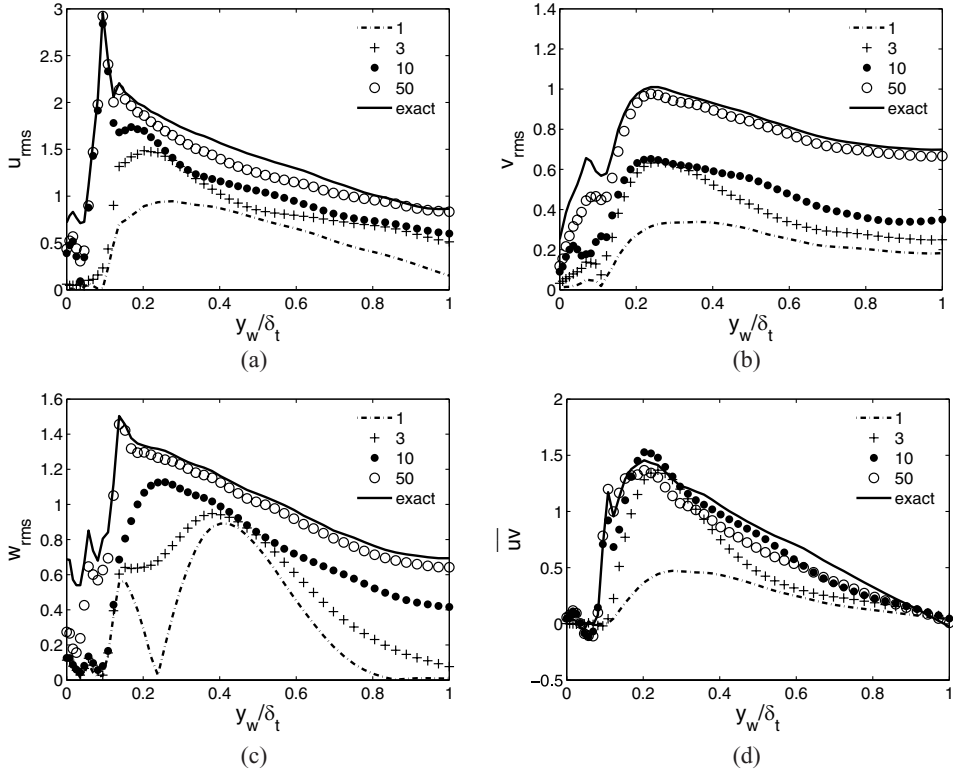
Figure 7. Reconstruction using 1, 3, 5, 10 and 50 POD modes of (a) rms of u, (b) rms of v, (c) rms of w, (d) uv (Reynolds stress).

A qualitative estimate of the character of the structures, in particular their streamwise and spanwise coherence, is obtained from the two-point correlations.

An analysis of two-point correlations has revealed a modification of the average diameter of the near-wall streamwise vortices as well as streak spacing. Figure 8 shows two-point correlations of the streamwise and wall-normal velocity components separated in the spanwise direction. The separation distance is normalized by the wall variables using the local wall-shear velocity. The two-point correlation for the streamwise velocity, R_{uu}, indicates that the streak spacing is increased to 140 wall units for the rough-wall case from the 100 wall units for the smooth-wall case at $y^+ = 30$. A similar trend of increased streak spacing is observed at $y^+ = 80$. Likewise, the two-point correlations of the wall-normal velocity, R_{vv}, indicates that the average diameter of the near-wall streamwise vortices is increased from 30 to 45 wall units at $y^+ = 30$, and a similar increase is observed at $y^+ = 80$. When the separation distance is normalized by the channel half height, no discernible difference between the smooth- and rough-wall cases is seen in the two-point correlations.

Figure 9 shows ϕ_u component of the first mode plotted in wall units in the y^+–z^+ plane for the rough wall (upper figure) and the smooth wall (lower figure). The rough-wall structures are further away from the wall compared to the smooth-wall structures. These structures are centered in the valley regions of the roughness bumps. The size of these structures increases in the spanwise direction for the rough wall compared to the smooth wall. The structures are elongated in the y direction. This appears to be consistent with the trend observed from the two-point correlations of the streamwise velocity component. Figure 10 shows the second POD mode. The rough-wall structures are centered in the valley regions of the roughness
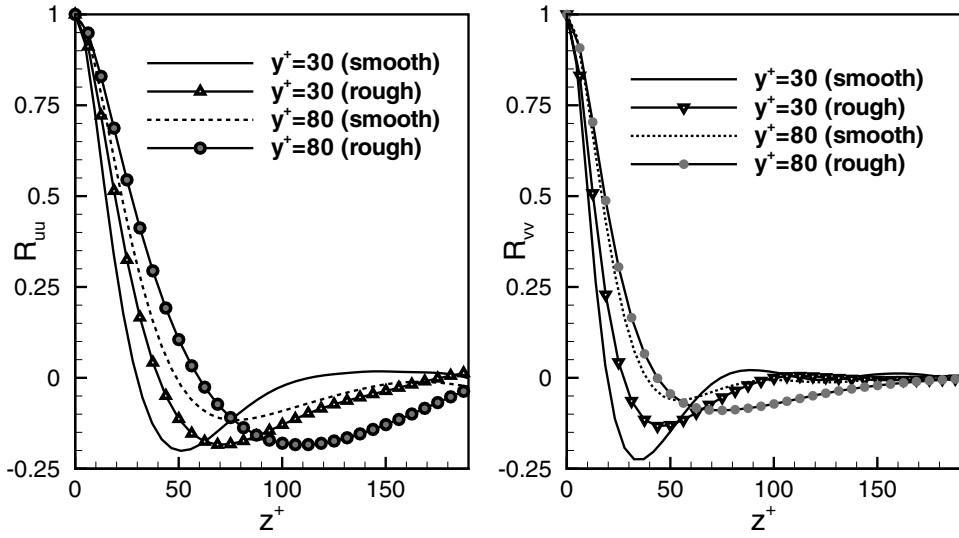
Figure 8. Two-point correlations separated in the spanwise direction with the spanwise distance normalized by wall variables.

bumps, similar to the first mode. Unlike the first mode, the size of the structures decreases in the spanwise direction for the rough wall. Figure 11 shows the third mode. The spanwise and wall-normal size of the structures for the rough wall are more or less similar to the size of the structures for the smooth wall. However, the structures for the rough wall are displaced away from the rough wall.
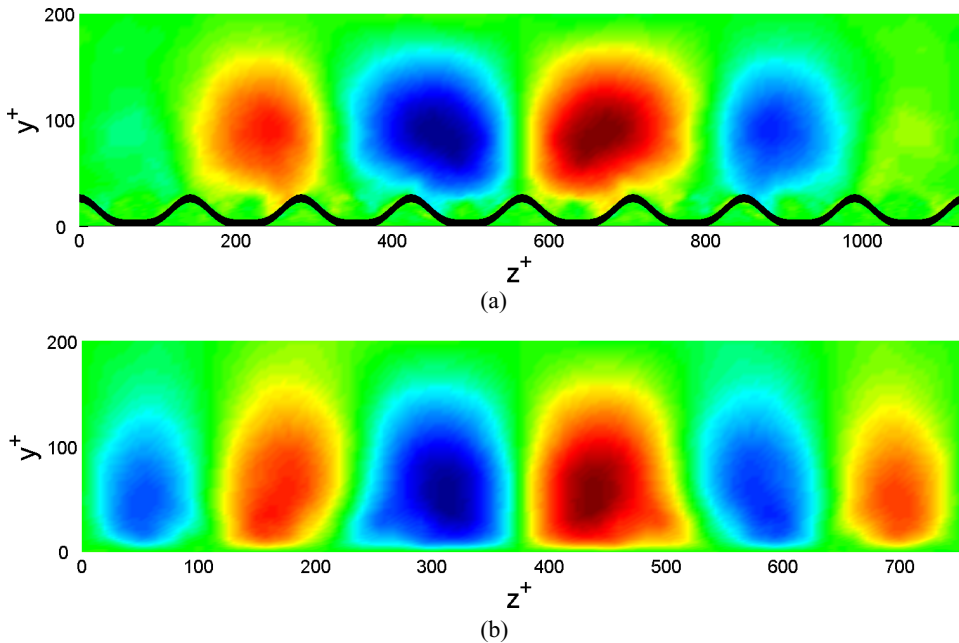

Figure 9. ϕ_u component of the first mode obtained from 2D y–z POD decomposition plotted in wall units for (a) rough wall, (b) smooth wall.

(a)

(b)

Figure 10. ϕ_u component of the second mode obtained from 2D y–z POD decomposition plotted in wall units for (a) rough wall, (b) smooth wall.

(a)

(b)

Figure 11. ϕ_u component of the third mode obtained from 2D y–z POD decomposition plotted in wall units for (a) rough wall, (b) smooth wall.
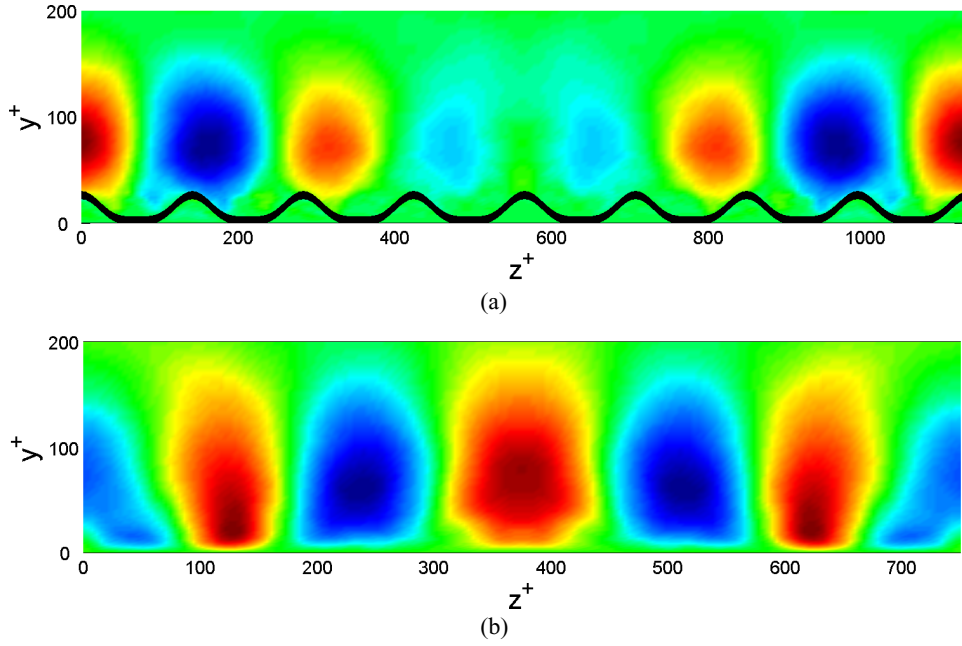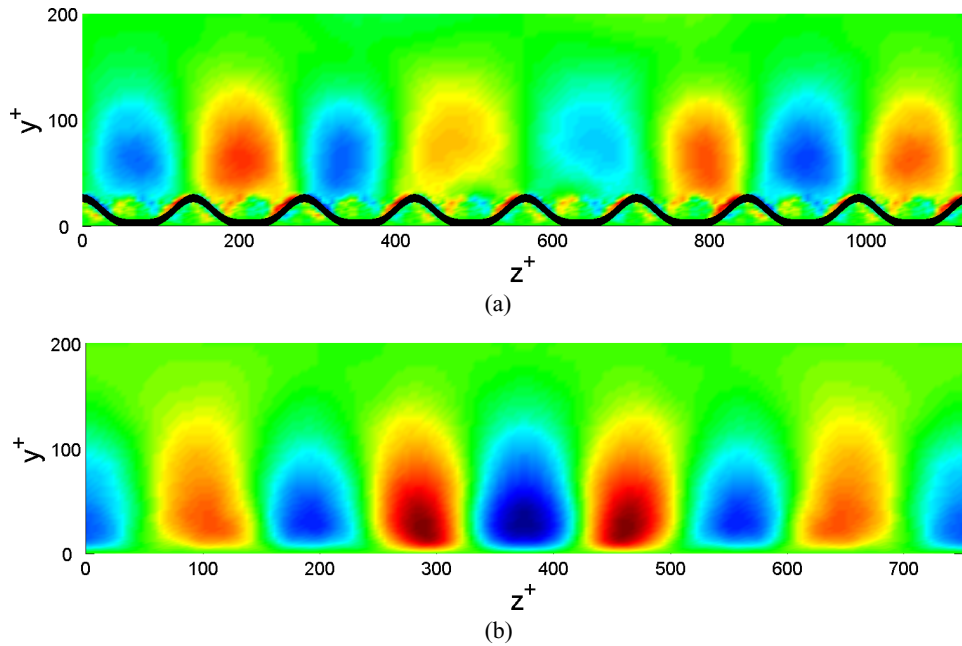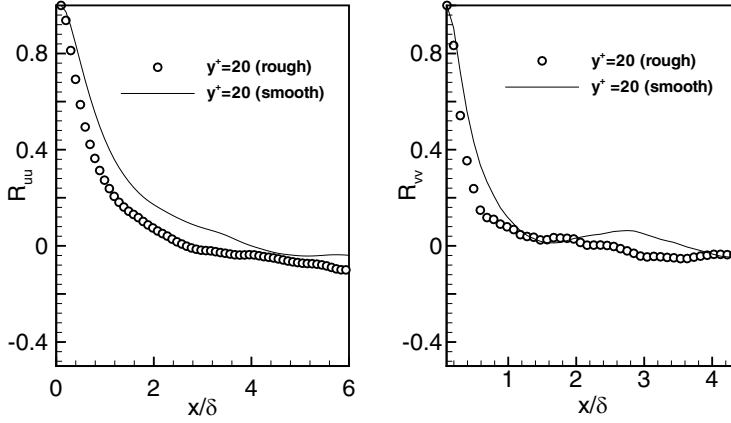
Figure 12. Two-point correlations separated in the streamwise direction with the spanwise distance normalized by channel half-height.

Likewise, to get an estimate of the nature of the structures in the streamwise direction, we perform 2D POD in the $x-y$ direction and compare the dominant streamwise modes for the rough- and smooth wall. We first estimate the streamwise extent of these structures based on the two-point correlations separated in the streamwise directions. Figure 12 shows R_{uu} and R_{vv} separated in the streamwise direction at two different wall-normal distance of $y^+ = 30$ and $y^+ = 80$. The separation distance is normalized by the channel half-height. The length of the streaks decreases for the rough-wall case. When the separation distance is normalized by the wall variables, no significant differences are observed.

Figure 13 shows the first POD mode for the rough- and smooth walls in the $x-y$ plane. The structures are further away from the rough wall compared to the smooth wall structures. Consistent with the analysis from the two-point correlations separated in the streamwise direction, the size of the structures decreases for rough wall compared to smooth wall. Figure 14 shows the second POD mode. Unlike the first mode, the streamwise size of the second mode is larger for the rough wall compared to the smooth wall.

The 2D POD analysis in the $y-z$ and $x-y$ planes suggests that energy containing structures of the rough wall are significantly modified compared to the smooth wall. Moreover, the first and the second POD modes exhibit significant structural differences. Significant structural differences between the rough- and smooth wall are not observed for higher modes.
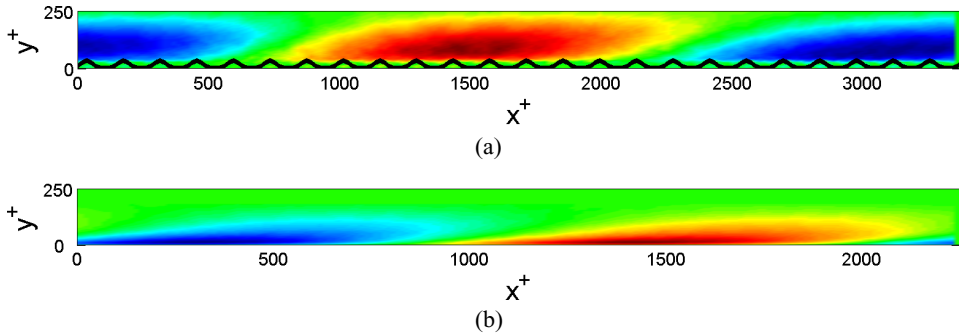

Figure 13. ϕ_u component of the first mode obtained from 2D $x-y$ decomposition for (a) rough wall, (b) smooth wall.
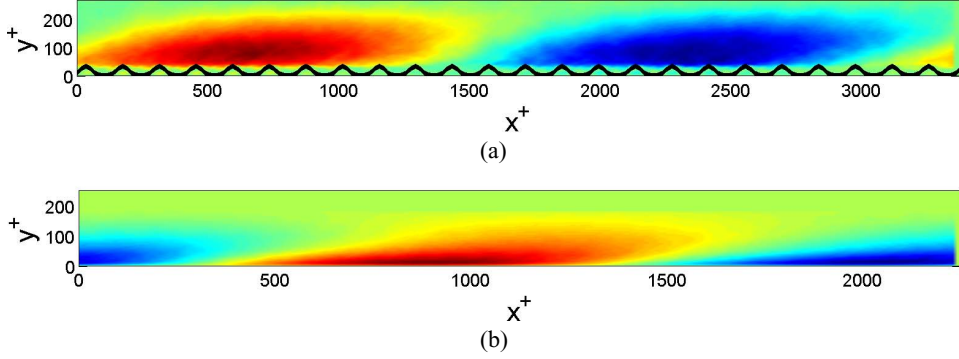
Figure 14. ϕ_u component of the second mode obtained from 2D $x-y$ decomposition for (a) rough wall, (b) smooth wall.

4. Discussion

The effect of surface roughness in a turbulent channel flow has been studied using snapshot POD analysis. The velocity database used is obtained from the DNS simulation of channel with a 'egg-carton' (double sinusoidal) roughness surface at $Re_\tau = 180$. The two-point correlations have been constructed from the DNS database. One dimensional POD analysis in the y direction has revealed that the convergence of POD modes obtained for the rough wall is slower compared to smooth wall. The first three modes capture around 35% and 50%, respectively, for the rough- and smooth walls. The first 10 modes capture around 70% and 80%, respectively, for the rough- and smooth walls. Finally, 90% of the total turbulent kinetic energy is captured by 22 modes for the rough wall and around 10 modes for the smooth wall. This trend and the slow convergence of the POD modes obtained for the rough wall can be attributed to an increase in the range of length scales due to roughness. It should be noted that even though the number of modes to reconstruct the flow for a rough wall is higher than the smooth wall, nevertheless, it is still a small fraction of the total number of modes, thus justifying POD as an effective tool to study the physics of a rough-wall turbulent boundary layer.

POD allows us to evaluate the distribution of energy as a function of scale. It decomposes the flow field into modes having various scales. POD captures the patterns (structures) that contribute to the TKE. A slower convergence signifies an increase in the number of structures that contain the total TKE for the rough wall. It should be noted that the dominant modes are still a large-scale structure as they capture significantly a large fraction of the TKE—18% (first mode), 10% (second mode) and 9% (third mode) of the TKE. One of the reasons for the generation for structures of various length scales is due to the kinematics of the roughness elements. Specifically, at the roughness valleys, the recirculation results in breakdown of the structures resulting in smaller length scales. The slower convergence thus represents the presence of additional length scales which are significant as they carry a sizable fraction of the TKE.

The depth of the roughness sublayer has been obtained by performing the 1D POD analysis at the peak and valley locations of the roughness bumps. We obtained the depth of the sublayer for the first mode ζ_{mode}^1 to be $6h$, h is the height of the roughness. The depth for second (ζ_{mode}^2), third (ζ_{mode}^3) and fourth (ζ_{mode}^4) modes are $2h$, $1.6h$ and $1.1h$. The depth of the sublayer decays with increasing mode number in an exponential manner. $\zeta_{\text{mode}}^n = 14he^{-0.86n}$, where the coefficients of the exponent have been obtained by data fitting.

In a parallel effort to study the structural effects of turbulence, quadrant analysis was performed by Krogstad *et al.* [26]. It was shown that the effect of roughness is extended upto $y = 5h$. The extent of influence of roughness on the dominant POD mode, ζ_{mode}^1 of $6h$ is slightly higher, but close to that revealed by their quadrant analysis. The large-scale features of flow based on velocity and pressure statistics were analyzed by Bhaganagar *et al.* [11, 12]. It was shown depth of the roughness sublayer ζ_q (obtained from velocity fluctuations) to be $1.5h$ and ζ_p (obtained from pressure fluctuations) to be $2h$. The roughness sublayer based on the dominant turbulence structures is nevertheless significantly larger than ζ_p or ζ_q.

The turbulent stresses have been reconstructed using the first few POD modes. The location and the amplitude of the peak of the rms of u fluctuations is well captured by the first 10 POD modes. The inner-layer, which included the roughness-sublayer, is well captured by these 10 POD modes. Adding additional POD modes does not change the inner-layer significantly. This confirms our findings regarding the roughness-sublayer that effect of inhomogeneity is captured by the lower modes. A similar trend is observed in the rms of v and w fluctuations and shear-stress uv.

A 2D POD analysis in the $y-z$ plane revealed that for the rough wall the dominant mode has increased the length scale in the spanwise direction compared to the smooth wall, whereas the second mode has a smaller spanwise length scale. Likewise, 2D analysis in the $x-y$ plane revealed that the streamwise length scale of the dominant mode is reduced for a rough wall, whereas the second mode has a larger length scale compared to the smooth wall.

The 2D POD analysis in the $y-z$ and $x-y$ planes suggest that energy containing structures of the rough wall are significantly modified compared to the smooth wall. Roughness alters the length scales of the dominant structures. The structures are further away from the rough wall compared to the smooth-wall structures. In particular, the first and the second POD modes exhibit structural differences. Sigificant structural differences between the rough- and smooth wall are not observed for higher modes. It appears to be consistent with our 1D analysis that rough alters predominantly the lower, energy containing structures of the flow.

The present analysis is restrictive to 3D egg-carton roughness elements selected for this study. Further work needs to be performed to understand the influence of roughness geometry, such as the size of roughness elements, height and spacing between the roughness elements, and 2D versus 3D roughness elements, on POD modes. Future investigation needs to be performed to extract three-dimensional coherent structures to better understand the effect of roughness.

References

[1] Antonia, R.A. and Krogstad, P.A., 2001, Return to isotropy for rough case using Lumley's triangle. *Fluid Dynamics Research* **28**, 139–157.

[2] Ashrfian, A. and Andersson, H., 2003, DNS of turbulent flow in a rod-roughened channel. *3 International Symposium on Turbulence and Shear Flow phenomena*, **1**, 117–122, Sendai, Japan, 25–27 June.

[3] Alfonsi, G. and Primavera, L., 2003, Coherent structures of the flow around a surface-mounted cubic obstacle in turbulent channel flow. *Journal of Wind Engineering and Industrial Aerodynamics*, **91**(4), 495–511.

[4] Aubry, N., Holmes, P., Lumley, J. L. and Stone, E., 1988, The dynamics of coherent structures in the wall region of a turbulent boundary layer. *Journal of Fluid Mechanics*, **192**, 115–173.

[5] Bandyopadhyay, R. and Watson, R.D., 1988, Structure of rough-wall turbulent boundary layers. *Physices of Fluids* **31**, 1877–1880.

[6] Bakewell, H.P. and Lumley, J.L., 1967, Viscous sublayer and adjacent wall region in turbulent pipe flow. *Phys. Fluids* **10**, 1880–1889.

[7] Ball, K.S., Sirovich, L. and Keefe, L.R., 1991, Dynamical eigenfunction decomposition of turbulent channel flow. *International Journal for Numerical Methods in Fluids*, **12**, 585–604.

[8] Berkooz, G., Holmes, P. and Lumley, J. L., 1991, Intermittent dynamics in simple models of the turbulent wall layer. *Journal of Fluid Mechanics*, **230**, 75–95.

[9] Berkooz, G., Holmes, P. and Lumley, J. L., 1993, The Proper Orthogonal Decomposition in the Analysis of Turbulent Flows. *Annual Review in Fluid Mechanics*, **25**, 539–575.

[10] Bhaganagar, K., Rempfer, D. and Lumley, J. L., 2002, Direct Numerical Simulation of Spatial Transition to Turbulence using Fourth-Order Vertical Velocity Second-Order Vertical Vorticity Formulation. *Journal of Compution Physics*, **180**, 200–228.

[11] Bhaganagar, K., Kim, J. and Coleman, G., 2004, Effect of roughness on wall-bounded turbulence. *Flow, Turbulence and Combustion*, **72**, 463–492.

[12] Bhaganagar, K., Coleman, G. and Kim. J., 2007, Effect of roughness on pressure statistics. *Physics of Fluids*, **19**(2).

[13] Blake, W. K., 1969, Turbulent-boundary layer pressure fluctuations over rough walls. *Proceedings of the 78th Meeting of the Acoustical Society of America*, **45**.

[14] Cui, J., Patel, V. and Lin, C. L., 2003, Large-eddy simulation of turbulent flow in a channel with rib roughness. *International Journal of Heat and Fluid Flow*, **24**(3), 372–388.

[15] Cheng, H. and Castro, I. P., 2002, Near wall flow over urban-like roughness. *Boundary-Layer Meteorology*, 229–257.

[16] Choi, K. S., 1989, Near wall structures of a turbulent boundary layer with riblets. *Journal of Fluid Mechanics*, **208**, 417–458.

[17] Faruya, F., 1976, Turbulent boundary layer and flow resistance on plates roughned by wires. *Journal of Fluid Engineering*, **98**(4), 635–644.

[18] George, J. and Simpson, R. L., 2000, Some effects of sparsely distributed three-dimensional roughness elements on two-dimensional turbulent boundary layers. *AIAA Paper*, 2000–0915.

[19] Hilberg, D., Lazik, W. and Fiedler, H. E., 1994, The application of Classical POD and Snapshot POD in a Turbulent Shear Layer with Periodic Structures. *Applied Scientific Research*, **53**, 283–290.

[20] Herzog, S., The large scale structures in the near-wall region of turbulent pipe flow. *PhD Thesis*, Cornell University, 1986.

[21] Jimenez, J., 2004, Turbulent flows over rough walls. *Annual Review of Fluid Mechanics*, **36**, 173–196.

[22] Juttijudata, V., Lumley, J. L. and Rempfer, D., 2005, Proper orthogonal decomposition in Squire's coordinate system for dynamical models of channel turbulence. *Journal of Fluid Mechanics*, **534**, 195–225.

[23] Keirsbulck, L., Mazouz, A., Labraga, L. and Tournier, C., 2001, Influence of the surface roughness on the third-order moments of velocity fluctuations. *Experimentals in Fluids* **30**, 592–594.

[24] Kostas, J., Soria, J. and Chong, M. S., 2005, A comparison between snapshot analysis of PIV velocity and vorticity data. *Experiments in Fluids*, **38**, 146–160.

[25] Krogstad, P., Antonia, R. A. and Browne, W. B., 1992, Comparison between rough-and smooth-wall turbulent boundary layers. *Journal of Fluid Mechanics*, **245**, 599–610.

[26] Krogstad, P. A., Andersson, H. I., Bakken, O. M., and Ashrafian, A., 2005, An experimental and numerical study of channel flow with rough walls. *Journal of Fluid Mechanics*, **530**, 327–352.

[27] Leonardi, S., Orlandi, P., Smalley, R., Djenidi. L. and Antonia, R., 2003, Direct Numerical Simulations of turbulent channel flow with transverse square bars on one wall. *Journal of Fluid Mechanics*, **491**, 229–238.

[28] Liu, Z., Adrian, R. J. and Hanratty, T. J., 2001, Large-scale modes of turbulent channel flow: transport and structure. *Journal of Fluid Mechanics*, **448**, 53–80.

[29] Liu, Z., Adrian, R. J. and Hanratty, T. J., 1994, Reynolds number similarity of orthogonal decomposition of the outer layer of turbulent wall flow. *Physics Fluids*, **6**(8), 2815–2819.

[30] Love, M. M., 1955, *Probability Theory*, Princeton, NJ: van Nostrand.

[31] Lumley, J. L., 1970, *Stochastic tools in Turbulence*, New York: Academic.

[32] Lumley, J. L., 1967, The structure of inhomogeneous turbulent flows, *Proceedings of the International Colloquium on the Fine-Scale Structure of the Atmosphere and its Influence on Radio Wave Propagation*, pp. 166–178, Nauka, Moscow.

[33] Lumley, J. L., 1981, Coherent structures in turbulence, *Transition and Turbulence*, New York, Academic, pp. 215–245.

[34] Manhart, M. and Wengle, H., 1993, A spatiotemporal decomposition of a fully inhomogeneous turbulent flow field. *Theoretical Computational Fluid Dynamics*, **5**, 223–242.

[35] Miyake, Y., Tsujimoto, K. and Nagai, N., 2002, Numerical simulation of channel flow with a rib-roughened wall. *Journal of Turbulence*, 1–10.

[36] Miyamoto, H. and Kanda, T., 2006, Multiresolutional-proper orthogonal hybrid analysis on turbulent structures in open-channel complex geometry flows. *International Journal of Wavelets, Multiresolution and Information Processing*, **4**(2), 297–310.

[37] Moin, P. and Moser, R.D., 1989, Characteristic-eddy decomposition of turbulence in a channel. *Journal of Fluid Mechanics*, **200**, 471–509.

[38] Mulhearn, P.J., 1976, Turbulent boundary layer wall-pressure fluctuations downstream from an abrupt change in surface roughness, *Physics of Fluids*, **19**(6), 796–801.

[39] Orlandi, P., Leonardi, S. and Tuzi, R., 2003, Direct numerical simulation of turbulent channel flow with wall velocity disturbances. *Physics of Fluids*, **15**(12), 3587–3601.

[40] Orlandi, P., Leonardi, S., and Antonia, R. A., 2006, Turbulent channel flow with either transverse or longitudinal roughness elements on one wall Source. *Journal of Fluid Mechanics*, **561**, 279–305.

[41] Orlandi, P. and Leanoardi, S., 2006, DNS of turbulent channel flows with two- and three-dimensional roughness. *Journal of Turbulence*, **7**, 1–22.

[42] Orellano, A. and Wengle, H., 2001, POD analysis of coherent structures in forced turbulent flow over a fence. *Journal of Turbulence*, **2**, 1–35.

[43] Perry, A. E., Lim, K. L. and Henbest, S. M., 1987, An experimental study of the turbulence structure in smooth- and rough-wall boundary layers. *Journal of Fluid Mechanics*, **177**, 437–466.

[44] Raupach, M. R., Antonia, R.A. and Rajagopalan, S., 1991, Rough-wall turbulent boundary layers. *Applied Mechanics Reviews*, **44**(1), 1–20.

[45] Sirovich, L., 1989, Chaotic dynamics of coherent structures. *Physics D*., **37**, 126–145.

[46] Sirovich, L., 1997, Dynamics of coherent structures in wall bounded turbulent turbulence. In R. L. Panton (Ed.), *Self-Sustaining Mechanisms of Wall Turbulence*, pp. 333–364, Southampton: Computational Mechanics Publications.

[47] Sirovich, L., 1987, Turbulence and the dynamics of coherent structures, Part 1: Coherent structures, Part 2: Symmetries and transformations, Part 3: Dynamics and scaling, *Quarterly of Applied Mathematics*, **5**, 561–590.

[48] Sirovich, L., Ball, K. S. and Handler, R. A., 1991, Propagating Structures in Wall-Bounded Turbulent Flows. *Theoretical and Computational Fluid Dynamics*, **2**, 307–317.

[49] Sirovich, L. and Rodriguez, J. D., 1987, Coherent structures and chaos: A model problem. *Physics Letters*, **A120**, 211.

[50] Shafi, H. S. and Antonia, R. A., 1997, Small-scale characteristics of a turbulent boundary layer over a rough wall. *Journal of Fluid Mechanics*, **342**, 263–293.

[51] Tachie, M. F., Bergstrom, D. J. and Balachandar, R., 2000, Rough wall turbulent boundary layers in shallow open channel flow. *Journal of Fluids Engineering*, **122**, 533–540.

[52] Thomas, A. and Bull, M., 1983, On the role of wall pressure fluctuations in deterministic motions in the turbulent boundary layer. *Journal of Fluid Mechanics*, **128**, 283.

[53] Waclawczyk, M. and Pozorski, J., 2002, Two-point velocity statistics and the POD analysis of the near-wall region in a turbulent channel flow. *Journal of Theoretical and Applied Mechanics*, **40**(4), 895–916.

[54] Webber, G. A., Handler, R. A. and Sirovich, L., 1997, The Karhunen–Love decomposition of minimal channel flow. *Physics Fluids*, **9**, 1054.

[55] Wood, N. and Mason, P., 1993, The pressure force induced by neutral turbulent flow over hills. *Quarterly Journal of the Royal Meteorological Society*, **119**, 1233–1267.

[56] Yusof, J. M., 1997, Combined immersed-boundary/B-spline methods for simulations of flow in complex geometries. *CTR-Annual Research Briefs*, Stanford Univ./NASA Ames.